

Supporting Information for: Water pressure fluctuations control variability in sediment flux and slip dynamics beneath glaciers and ice streams

A. Damsgaard, L. Goren, and J. Suckale

anders@adamsgaard.dk

Supplementary Note 1. Methods

GDR-MiDi (1) presented a non-dimensional inertia number that summarizes the mechanical behavior of dry and dense granular deformation. The rate dependence on mechanical properties evolved into an empirical continuum rheology in (2) and (3), where apparent friction and porosity depend on the inertia number. However, these models are *local*, meaning that local stresses determine the local strain-rate response alone. As a consequence, material properties do not influence shear zone width, which is not consistent with observations (1, 4–6). Granular deformation contains numerous non-local effects, where flow rates in neighboring areas influence the tendency of a sediment parcel to deform. Granular shear zones are an example of the non-locality as they have a minimum width dependent on grain characteristics (7–9).

Original non-local granular fluidity (NGF) model

Henann and Kamrin (10) presented the non-local granular fluidity (NGF) model where a *fluidity* field variable accounts for the non-local effects on deformation. The model builds on previous continuum rheologies for granular materials (2, 3) and accurately describes non-local strain distribution in a variety of experimental settings. The physical basis for the NGF model is the statistics of a kinetic elasto-plastic mechanism, which envisions mesoscopic regions undergoing localized yielding and inducing elastic deformation in nearby, jammed regions. The consequence is a non-local picture of the flow that is characterized by a finite cooperation length. Fluidity acts as a state variable, describing the phase transition between non-deforming (jammed) and actively deforming (flowing) regions in the sediment (10, 11). All material is assumed to have a uniform porosity and to be in the critical state. The modeled sediment deforms with yield beyond the Mohr-Coulomb failure limit (10, 12), but unlike classical plastic models it includes a closed form relation that predicts the stress-strain rate relation at and slightly beyond yield.

In the NGF model, shear deformation is contributed by elastic ($\dot{\gamma}^e$) and plastic ($\dot{\gamma}^p$) shear strain rate :

$$\dot{\gamma} = \dot{\gamma}^e + \dot{\gamma}^p \quad (1)$$

where the plastic contribution to shear strain rate is given by:

$$\dot{\gamma}^p = g(\mu, \sigma_n)\mu. \quad (2)$$

Here, $\mu = \tau/\sigma_n$ is the dimensionless ratio between shear stress (τ [Pa]) and normal stress (σ_n [Pa]), and g [s^{-1}] is the granular fluidity. The fluidity g is a kinematic variable governed by grain velocity fluctuations and packing fraction (11), and consists of local and non-local components:

$$\nabla^2 g = \frac{1}{\xi^2(\mu)}(g - g_{\text{local}}), \quad (3)$$

The degree of non-locality is scaled by the cooperativity length ξ [m], which, in turn, scales with non-local amplitude A [-]:

$$\xi(\mu) = \frac{Ad}{\sqrt{|\mu - \mu_s|}}, \quad (4)$$

where d [m] is the representative grain diameter and μ_s [-] is the static Coulomb yield coefficient. The local contribution to fluidity is defined as:

$$g_{\text{local}}(\mu, \sigma_n) = \begin{cases} \sqrt{d^2 \sigma_n / \rho_s} (\mu - \mu_s) / (b \mu) & \text{if } \mu > \mu_s, \text{ and} \\ 0 & \text{if } \mu \leq \mu_s. \end{cases} \quad (5)$$

where ρ_s [kg m⁻³] is grain mineral density, and b [-] controls the non-linear rate dependence beyond yield. The failure point is principally determined by the Mohr-Coulomb constituent relation in the conditional of Eq. 5. However, the non-locality in Eq. 3 implies that deformation can occur in places that otherwise would not fail, in cases where the surrounding areas have a high local fluidity.

Numerical solution procedure

We solve the cohesive non-local granular fluidity model with pore fluid (CNGF-PF) equations in a one-dimensional setup where simple shear occurs along a horizontal axis x , orthogonal to a vertical axis z . The spatial domain is $L_z = 8$ m long and is discretized into cells with equal size to the representative grain size d . The upper boundary, i.e. the ‘‘ice-bed interface’’, exerts effective normal stress and shear stress on the granular assemblage. We neglect the minuscule contribution to material shear strength from water viscosity. The effective normal stress within the layer is found by adding the lithostatic contribution that increases with depth to the normal stress applied from the top:

$$\sigma_n(z) = \sigma_{n,\text{top}} + (1 - \phi) \rho_s G (L_z - z), \quad (6)$$

where G [m s⁻²] is gravitational acceleration, and

$$\sigma'_n(z) = \sigma_n(z) - p_f(z). \quad (7)$$

Normal stress $\sigma_n(z = L_z)$ and fluid pressure $p_f(z = L_z)$ at the top are described by the boundary condition as constant or time-variable values. The shear stress τ is constant over the domain, while effective normal stress varies. We compute the apparent friction coefficient μ , which is the ratio between shear and effective normal stress, as:

$$\mu(z) = \mu_{0,\text{top}} \frac{\sigma'_{n,\text{top}}}{\sigma'_n(z)}. \quad (8)$$

where $\mu_{0,\text{top}}$ is the initial friction at the top at $t = 0$. The shear stress $\tau(z) = \mu(z) \sigma'_n(z)$ is constant in time and space for stress-controlled experiments, and dynamic for speed-controlled experiments.

We assign depth coordinates z_i , granular fluidity g_i , and fluid pressure $p_{f,i}$ to a regular grid with ghost nodes and cell spacing Δz . The ghost nodes are imaginary grid nodes outside of the top and bottom boundaries, and their values are dynamically adjusted to provide the desired boundary condition. The fluidity field g is solved for a set of mechanical forcings (μ , σ'_n , boundary conditions for g), and material parameters (A , b , d). We rearrange Eq. 3 and split the Laplace operator (∇^2) into a 1D central finite difference 3-point stencil. We apply an iterative scheme to relax the following equation at each grid node i :

$$g_i = (1 + \alpha_i)^{-1} \left(\alpha_i g_{\text{local}}(\sigma'_{n,i}, \mu_i) + \frac{g_{i+1} + g_{i-1}}{2} \right), \quad (9)$$

where

$$\alpha_i = \frac{\Delta z^2}{2 \xi^2(\mu_i)}. \quad (10)$$

We apply fixed-value (Dirichlet) boundary conditions for the fluidity field ($g(z = 0) = g(z = L_z) = 0$). This condition is appropriate for confined flows. Neumann boundary conditions, which are not used here, create a velocity profile resembling a free surface flow.

The pore-pressure solution (Eq. 3 in the main text) is constrained by a hydrostatic pressure gradient at the bottom ($dp_f/dz(z = 0) = \rho_f G$), and a pressure forcing at the top, for example sinusoidal: $p_f(z = L_z) = A_f \sin(2\pi f t) + p_{f,0}$. Here, A_f is the forcing amplitude [Pa], f is the forcing frequency [1/s], and $p_{f,0}$ is the mean pore pressure over time [Pa]. As for the granular fluidity field (Eq. 3), we also use operator splitting and finite differences to solve the equation for pore-pressure diffusion (Eq. 3 in the main text):

$$\Delta p_{f,i} = \frac{1}{\eta_f(\alpha + \phi_i \beta_f)} \frac{\Delta t}{\Delta z} \left(\frac{2k_{i+1}k_i}{k_{i+1} + k_i} \frac{p_{i+1} - p_i}{\Delta z} - \frac{2k_i k_{i-1}}{k_i + k_{i-1}} \frac{p_i - p_{i-1}}{\Delta z} \right). \quad (11)$$

For each time step Δt , we compute a solution to Eq. 11 through the Crank-Nicholson method (13–15). In this procedure, the pressure field at $t + \Delta t$ is found by mixing explicit and implicit solutions with equal weight. The method is unconditionally stable and second-order accurate in time and space. Our implementation of grain and fluid dynamics is highly efficient, and for the presented experiments each time step completes in less than 1 ms on a single CPU core.

Speed-controlled experiments

The model form presented above is suited for resolving strain rate and shear velocity from a given stress forcing, i.e., in a stress-controlled setup. However, the basal conditions under glaciers and ice streams are highly variable and certain cases are better approximated by a speed-controlled limit where a specified shear speed at the interface results in a strain-rate distribution and shear stress inside the subglacial bed. For our system of equations, this case represents an inverse problem that we compute by adjusting the applied friction at the top until the resultant shear speed matches the desired value. We implement an automatic iterative procedure that can be set to match a shear speed, or limit the speed to a specified value. First, we calculate an initial top speed value v_x^* is calculated in a forward manner on the base of an arbitrary value for friction μ^* . We use the difference between v_x^* and the desired speed v_x^d in the calculation of a normalized residual r :

$$r = \frac{v_x^d - v_x^*}{v_x^* + 10^{-12}}. \quad (12)$$

We add the value 10^{-12} to the denominator to avoid division by zero if the initial applied friction value μ^* does not cause yield. If the residual value r is negative, the current applied friction produces a shear speed that exceeds the desired value, and vice versa. If the absolute value of the residual exceeds the tolerance criteria ($|r| > 10^{-3}$), we adjust the applied friction:

$$\mu_{\text{new}}^* = \mu^*(1.0 + \theta r), \quad (13)$$

where $\theta = 10^{-2}$ is a chosen relaxation factor. The computations are then rerun with the new applied friction until the tolerance criteria is met.

Supplementary Note 2. Analytical solution for maximum deformation depth

Under the assumption that the bed is a semi-infinite halfspace, we can solve for the depth profile and transient behavior of effective normal stress σ'_n analytically by extending a solution for dispersion of a sinusoidal forcing through a diffusive medium (16). Here, z' is the depth below the ice-bed interface, i.e., $z' = L_z - z$:

$$\sigma'_n(z', t) = \sigma_n + (\rho_s - \rho_f)Gz' - p_{f,\text{top}} - A_f \exp\left(-\frac{z'}{d_s}\right) \sin\left(\omega t - \frac{z'}{d_s}\right). \quad (14)$$

We compute the vertical gradient of the effective normal stress by evaluating,

$$\frac{d\sigma'_n}{dz'}(z', t) = (\rho_s - \rho_f)G + \frac{A_f}{d_s} \exp\left(-\frac{z'}{d_s}\right) \left[\sin\left(\omega t - \frac{z'}{d_s}\right) + \cos\left(\omega t - \frac{z'}{d_s}\right) \right], \quad (15)$$

where $\omega = 2\pi f$ is the circular forcing frequency [s^{-1}]. For this study, we want to find the depth z' where $d\sigma'_n/dz' = 0$. At this depth the effective normal stress is at a minimum and deep deformation can occur. In our simulations we observe that the deepest deformation occurs when water pressure is at its minimum at the ice-bed interface, which means that $t = 3\pi/2\omega$:

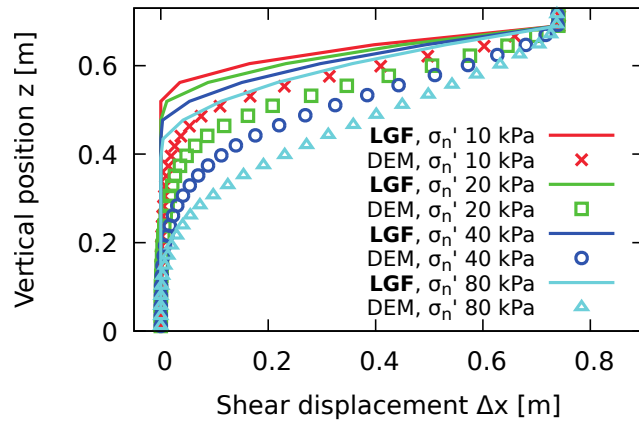
$$0 = \sin\left(\frac{3\pi}{2} - \frac{z'}{d_s}\right) + \cos\left(\frac{3\pi}{2} - \frac{z'}{d_s}\right) + \frac{(\rho_s - \rho_f)Gd_s}{A_f} \exp\left(\frac{z'}{d_s}\right) \quad (16)$$

In the main text, the above equation is presented in shorter form using the identity, $\sin(x) + \cos(x) = \sqrt{2} \sin(x + \pi/4)$. With a sinusoidal water-pressure forcing, the above equation has no solution if $d\sigma'_n/dz(z=0) > 0$. This is the case if the pressure perturbation is too weak to reverse the effective normal stress curve at depth, causing shear deformation to occur at the top throughout the water-pressure cycle.

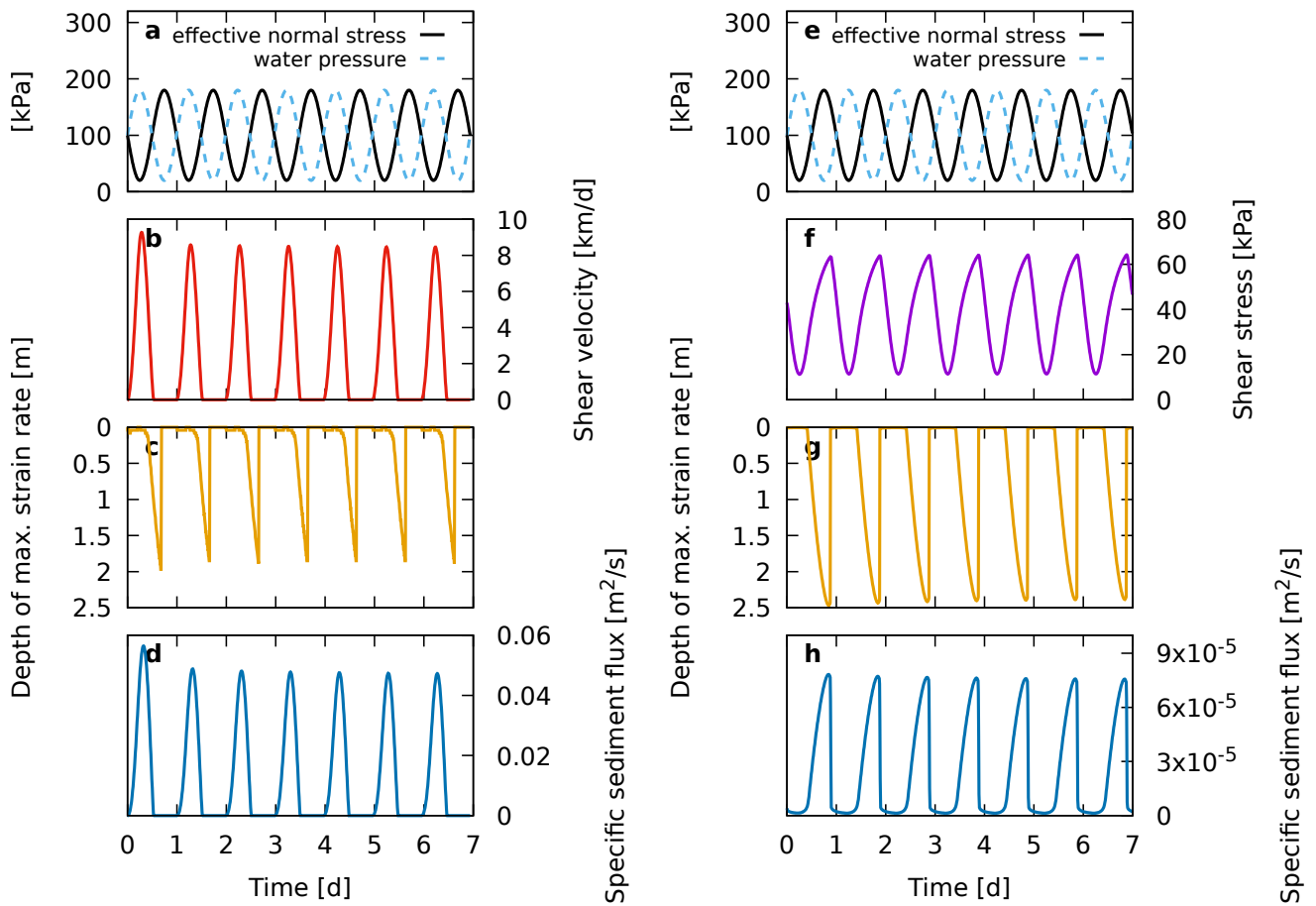
We use Brent's method (15) for numerically finding depth (z') values that satisfy the above equation within $z' \in [0; 5d_s]$. Our implementation, the program `max_depth_simple_shear`, takes command-line arguments of the same format as the main NGF program, `1d_fd_simple_shear`, and prints the maximum deformation depth (z') as the first column of output, and the skin depth (d_s) as the second column. See "`max_depth_simple_shear -h`" for usage details.

Supplementary Note 3. Parameter sensitivity test

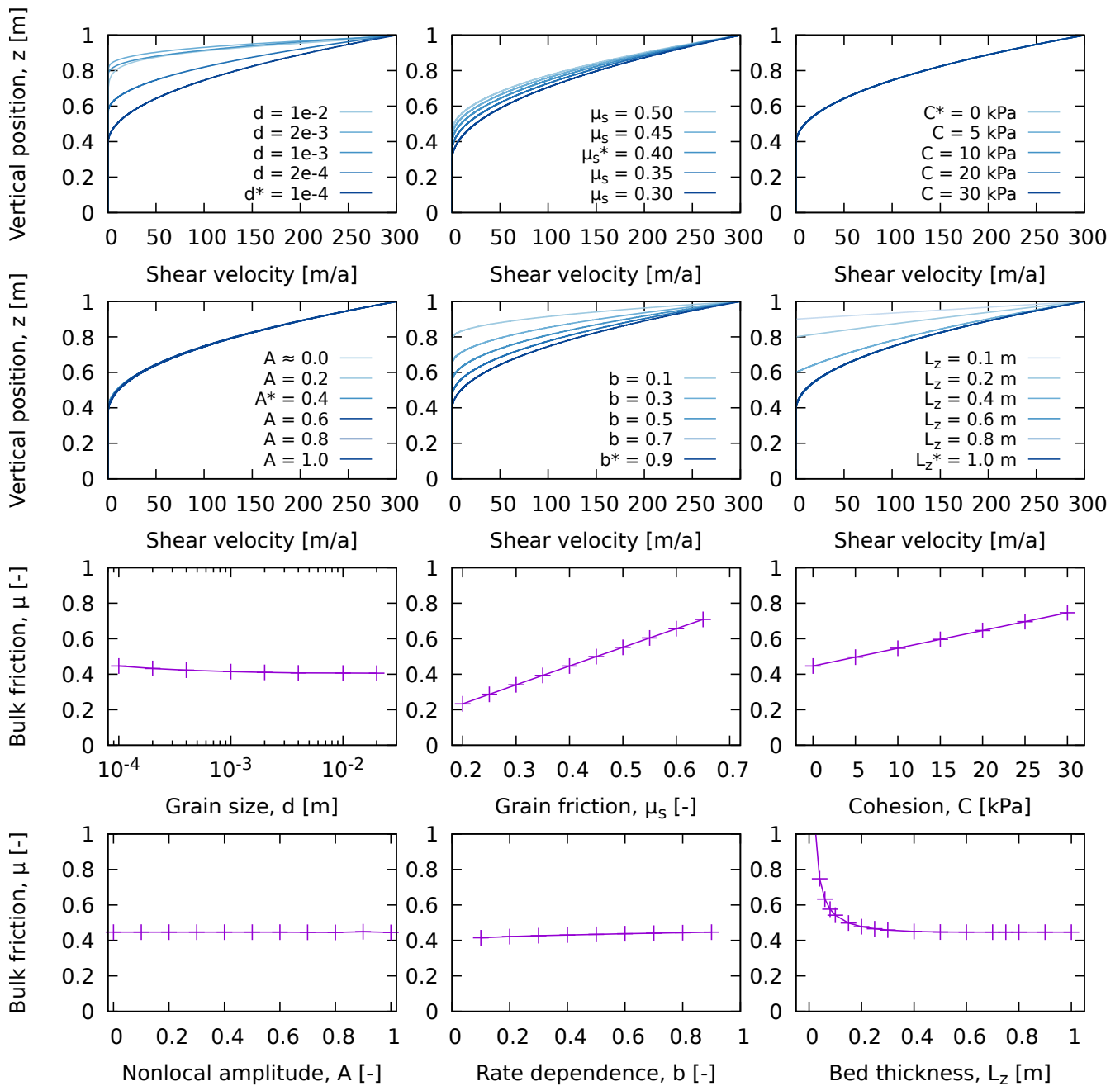
Supplementary Figure 3 contains a systematic analysis of parameter influence in the model equations. Several observations emerge from this parameter sensitivity analysis. The representative grain size d has a major influence on the strain distribution, where finer materials show deeper deformation. The material is slightly weaker with larger grain sizes. The shear zone is more narrow with higher material static friction coefficients (μ_s), as the material is less prone to failure. Our implementation of cohesion does not influence strain after yield. Static friction and cohesion both linearly scale the bulk friction, as expected with Mohr-Coulomb materials. The non-local amplitude A slightly changes the curvature of the shear strain profile, but does not affect the overall friction. There is a significant strengthening when the bed thickness L_z begins to constrict the shear zone thickness.



Supplementary Fig. 1. Strain distribution in local-only granular fluidity (LGF) model ($A \approx 0$).



Supplementary Fig. 2. Deformation dynamics during sinusoidal water-pressure forcing from the top. Stress and shear velocity are measured at the top of the sediment bed. a-d) Stress-controlled setup with applied shear stress $0.4\sigma'_n$. e-h) speed-controlled setup with applied shear velocity $v_x = 1 \text{ km/a}$.



Supplementary Fig. 3. Analysis of parameter influence on steady-state strain distribution and bulk friction during shear. All experiments are performed under constant shear rate of 300 m a^{-1} and a normal stress of $\sigma'_n = 100 \text{ kPa}$. Parameter values marked with an asterisk (*) are used outside of the individual parameter sensitivity tests.

Supplementary Table 1. Material parameters for model simulations emulating discrete element method (DEM) particles (17) (Fig. 1D), an idealized till (remaining figures), and West Antarctic Ice Sheet (WAIS) till. Parameter values from the literature are used where marked with a reference symbol: a: (17), b: (17), c: (12), d: (18), e: (19), f: (20).

Parameter	Symbol	Units	DEM particles	Idealized till	WAIS till
Friction coefficient	μ_s	—	0.404 _a	0.40	0.45 _f
Cohesion	C	kPa	0 _a	0	3 _f
Representative grain size	d	m	0.04	1.0×10^{-3}	1.0×10^{-3}
Hydraulic permeability	k	m^2	$2.1 \times 10_b^{-15}$	2.1×10^{-15}	—
Nonlocal amplitude	A	—	0.50	0.48 _c	0.48 _c
Nonlinear rate dependence	b	—	0.022	0.94 _c	0.94 _c
Grain material density	ρ_s	kg m^{-3}	$2.6 \times 10_a^3$	2.6×10^3	2.6×10^3
Porosity	ϕ	—	0.25 _a	0.25	0.35 _f
Dynamic fluid viscosity	η_f	Pa s	$1.787 \times 10_d^{-3}$	$1.787 \times 10_d^{-3}$	—
Pore-skeleton compressibility	α	Pa^{-1}	10^{-8}	10^{-8}	—
Adiabatic fluid compressibility	β_f	Pa^{-1}	$3.9 \times 10_e^{-10}$	$3.9 \times 10_e^{-10}$	—
Fluid diffusivity	D	$\text{m}^2 \text{s}^{-1}$	—	—	10_f^{-8}

References

- [1] GDR-MiDi. On dense granular flows. *Eur. Phys. J. E*, 14:341–365, 2004. doi: 10.1140/epje/i2003-10153-0.
- [2] F. da Cruz, S. Emam, M. Prochnow, J.-N. Roux, and F. Chevoir. Rheophysics of dense granular materials: Discrete simulation of plane shear flows. *Phys. Rev. E*, 72(2), 2005. doi: 10.1103/physreve.72.021309.
- [3] P. Jop, Y. Forterre, and O. Pouliquen. A constitutive law for dense granular flows. *Nature*, 441(7094):727–730, 2006. doi: 10.1038/nature04801.
- [4] D. M. Mueth, G. F. Debregeas, G. S. Karczmar, P. J. Eng, S. R. Nagel, and H. M. Jaeger. Signatures of granular microstructure in dense shear flows. *Nature*, 406(6794):385–389, 2000.
- [5] W. Losert, L. Bocquet, T. C. Lubensky, and J. P. Gollub. Particle dynamics in sheared granular matter. *Phys. Rev. Lett.*, 85(7):1428, 2000. doi: 10.1103/physrevlett.85.1428.
- [6] G. Koval, J.-N. Roux, A. Corfdi, and F. Chevoir. Annular shear of cohesionless granular materials: From the inertial to quasistatic regime. *Phys. Rev. E*, 79(2):021306, 2009. doi: 10.1103/physreve.79.021306.
- [7] R. M. Nedderman and C. Laohakul. The thickness of the shear zone of flowing granular materials. *Powder Technol.*, 25(1):91–100, 1980. doi: 10.1016/0032-5910(80)87014-8.
- [8] Y. Forterre and O. Pouliquen. Flows of dense granular media. *Ann. Rev. Fluid Mech.*, 40(1):1–24, 2008. doi: 10.1146/annurev.fluid.40.111406.102142.
- [9] K. Kamrin. Quantitative Rheological Model for Granular Materials: The Importance of Particle Size. In *Handbook of Materials Modeling*, pages 1–24. Springer International Publishing, 2018. doi: 10.1007/978-3-319-50257-1_148-1.
- [10] D. L. Henann and K. Kamrin. A predictive, size-dependent continuum model for dense granular flows. *Proc. Nat. Acad. Sci.*, 110(17):6730–6735, 2013. doi: 10.1073/pnas.1219153110.
- [11] Q. Zhang and K. Kamrin. Microscopic description of the granular fluidity field in nonlocal flow modeling. *Phys. Rev. Lett.*, 118(5), 2017. doi: 10.1103/physrevlett.118.058001.
- [12] D. L. Henann and K. Kamrin. A finite element implementation of the nonlocal granular rheology. *Int. J. Num. Meth. Eng.*, 108(4):273–302, 2016. doi: 10.1002/nme.5213.
- [13] S. V. Patankar. *Numerical Heat Transfer and Fluid Flow*. CRC Press, Boca Raton, Florida, 1980.
- [14] J. H. Ferziger and M. Perić. *Computational Methods for Fluid Dynamics*, volume 3. Springer, Berlin, 2002.
- [15] W. H. Press, S. A. Teukolsky, W. T. Vetterling, and B. P. Flannery. *Numerical recipes 3rd edition: The art of scientific computing*. Cambridge University Press, Cambridge, 2007.
- [16] D. L. Turcotte and G. Schubert. *Geodynamics*. Cambridge University Press, Cambridge, 2002. doi: 10.1017/cbo9780511807442.012.
- [17] A. Damsgaard, D. L. Egholm, J. A. Piotrowski, S. Tulaczyk, N. K. Larsen, and K. Tylmann. Discrete element modeling of subglacial sediment deformation. *J. Geophys. Res. Earth Surf.*, 118:2230–2242, 2013. doi: 10.1002/2013JF002830.
- [18] K. M. Cuffey and W. S. B. Paterson. *The Physics of Glaciers*. Elsevier, Amsterdam, 2010.
- [19] R. A. Fine and F. J. Millero. Compressibility of water as a function of temperature and pressure. *J. Chem. Phys.*, 59(10):5529–5536, 1973. doi: 10.1063/1.1679903.
- [20] S. Tulaczyk, W. B. Kamb, and H. F. Engelhardt. Basal mechanics of ice stream B, West Antarctica i. Till mechanics. *J. Geophys. Res.*, 105(B1):463–481, 2000. doi: 10.1029/1999JB900329.